nature communications

Article

https://doi.org/10.1038/s41467-024-51415-5

High-resolution flexible iontronic skins for both negative and positive pressure measurement in room temperature wind tunnel applications

Received: 1 January 2024

Accepted: 6 August 2024

Published online: 17 August 2024

Check for updates

Jingxiao Wang[1,2], Xueyong Wei[1,3] ✉, Junli Shi[2], Ningning Bai[2], Xiao Wan[1], Bing Li[1], Yingchun Chen[4] ✉, Zhuangde Jiang[1] & Chuan Fei Guo[2] ✉

Flexible skins that can be laminated on curved surfaces are a desired form for wind pressure measurement. Sensors for such applications need to detect both negative and positive wind pressure with ultrahigh pressure resolution over a wide range up to 600 kPa, whereas existing flexible sensors are unsatisfactory to such demands. Here, we report a flexible skin containing two iontronic pressure sensors for negative pressure and positive pressure sensing, respectively, and show the potential of the skin for pressure measurement in room temperature wind tunnels. We control the contact state of iontronic interface of a sensor to introduce a pre-pressure that enables negative pressure sensing, exhibiting a pressure resolution of −20 Pa (0.025%) within a broad pressure regime (from −100 kPa to −10 Pa). The other sensor for positive pressure sensing exhibits a pressure-resolution of 100 Pa (0.025%) over 600 kPa, in addition to a wide frequency bandwidth up to 400 Hz. The skin with the two types of sensors can be attached on curved surfaces of wing surface for pressure measurement at various free stream velocities and angles of attack. This study provides a promising technology of using flexible skins for pressure measurement in aviation applications.

Flexible skins that can be laminated on an aircraft model for pressure measurement and pressure mapping in a wind tunnel test is a promising technology for better design and the safety of aircrafts[1–3]. The surfaces of an aircraft or an aircraft model can experience dynamic and subtle changes in pressure caused by air turbulence, separation flow, shock wave interference, or other environmental conditions[4–8], for which real-time pressure distribution or change in pressure needs to be detected. Unlike pressure sensing in many other fields such as robotics and wearable healthcare[9–13], wind pressure sensing needs to measure both positive and negative pressure values from −100 to 600 kPa with a high pressure resolution of ~100 Pa because the surface pressure can be either higher or lower than the surrounding air pressure[14–16], determined by the wind velocity on the surface.

Traditional techniques for wind pressure measurements include pressure taps and pressure sensitive paints[17,18], both are popular in wind tunnel tests. The former is an invasive method involving in the puncture of small holes in wings or in the body, which connect to pressure transducers via slender tubes[19,20]. Furthermore, it is difficult to implant tubes at the trailing edges of wings, a critical location for air pressure measurement. The other technique, although being non-

[1]State Key Laboratory for Manufacturing Systems Engineering, Xi'an Jiaotong University, Xi'an 710049, China. [2]Department of Materials Science and Engineering, Southern University of Science and Technology, Shenzhen, Guangdong 518055, China. [3]School of Instrument Science and Technology, Xi'an Jiaotong University, Xi'an 710049, China. [4]Science and Technology Committee, Commercial Aircraft Corporation of China Ltd., Shanghai 200126, China. ✉e-mail: seanwei@xjtu.edu.cn; chenyingchun@comac.cc; guocf@sustech.edu.cn

invasive, needs to spray a pressure-sensitive luminescent material on the model surface and the colors are recorded by a set of cameras. However, this method suffers from the poor pressure-resolution and unstable performance in different weather conditions[21], and corners that are readily blocked cannot be monitored by the cameras. Recently, flexible pressure sensor-based skins, which can be laminated on curved surfaces, have been used to measure wind pressure[22–25]. However, existing sensors in such skins exhibit low sensitivity and a narrow working range of only a few kilopascals, and their applications are limited to small and low-speed unmanned aircraft or low speed wind tunnels[26–28].

Iontronic flexible pressure sensors, which use a layer of ionic soft material to replace common dielectric in capacitive sensors, are a class of emerging devices that exhibit ultrahigh sensitivity and a wide pressure response range[29–32]. An electric double layer (EDLs) forms when a low voltage is applied, with electrons in the electrode and the counter ions in the ionic gel gathering at the electrode-ionic soft material interface[33,34]. The capacitance signal of an iontronic sensor can be expressed as $C \approx \varepsilon A/d$, where ε is the permittivity, A is the interfacial contact area between the ionic gel and the electrode, and d is charge separation (~1 nm) between ions and electrons at the EDLs, which is much smaller than that of the distance between the two electrodes (mostly 10 μm ~ 100 μm)[35,36]. In iontronic sensors, ε and d are considered as invariants, and the magnitude of capacitive signal is determined only by the contact area between the ionic gel and the electrode, or $C \propto A$. Iontronic pressure sensors can achieve high sensitivity over a wide pressure range by elaborately designing microstructures with high compressibility[37,38]. Existing iontronic pressure sensors, however, fail to detect external negative pressure that commonly exists in the aerospace field.

Here, we report a skin containing two types of highly sensitive iontronic sensors that are designed to detect negative and positive pressure, respectively, for pressure sensing in plane models in room temperature wind tunnel tests. The negative pressure sensing is enabled by introducing a sealed cavity and a pre-pressure, and the sensor exhibits a pressure-resolution of −20 Pa (or 0.025%) over the full negative pressure regime. The sensor for detecting positive pressure exhibits a pressure-resolution of 100 Pa or 0.025% over 0–600 kPa. This sensor also exhibits a fast response-relaxation speed so that it can monitor vibrations up to 400 Hz. We further integrated the skin onto the NACA-0012 wing surface for pressure distribution test. A series of wind tunnel experiments were carried out for pressure tests under different free stream velocities (U_∞) or angles of attack (AOA).

Results

Principle and sensing mechanism of the flexible sensors

Air pressure is determined by wind velocity, according to Bernoulli's principle (Fig. 1a). The wind velocity is higher at the upper surface of the wing, causing a negative pressure on the upper wing surface and a positive pressure on the lower wing surface. The value of lift force is determined by pressure difference of the two surfaces. Therefore, unlike pressure sensing in robotics and healthcare, aviation applications require skins to detect negative pressure at the top surface and positive pressure at the bottom surface of wings.

Here, we design an iontronic sensor specifically for negative pressure detection at the upper surface, and another sensor for positive pressure sensing, termed S_n and S_p, respectively. Both sensors are based on the iontronic sensing mechanism, and sealed to have a chamber that has a pressure balanced by the surrounding air pressure (Fig.1b). Both S_n and S_p consist of four layers, including a microstructured top electrode of gold-coated polyimide membrane (PI-Au), a flat PI-Au bottom electrode, a microstructured ionic gel film placed between the two electrodes, and a spacer of polydimethylsiloxane (PDMS) that fixes the interlayer distance of the two electrodes.

The response to pressure of the sensor is determined by the device configuration and the microstructures of the electrode-ionic gel interface[39,40]. To determine an ideal output curve and elucidate the underlying mechanism, we investigated four representative structures (Supplementary Fig. 1a) by performing finite element analysis (FEA). These structures include planar-structured interfaces (planar-hemispheric array, and a planar-intrafillable microstructures) and bi-structured interfaces (domed-introfillable interface, and bi-intrafillable interface). The so-called "intrafillable structure", for which the protrusions can buckle and fill in the underlying pores and grooves, leads to high structure compressibility. Such a behavior helps achieve high sensitivity over a wide pressure range of the sensor[37]. The FEA results show that the bi-intrafillable interface exhibits the largest change in contact area in the high-pressure range (Supplementary Fig. 1b). That is, the combination of these two microstructures can further enhance the sensitivity as well as the pressure-response range, to satisfy the requirement of high pressure-resolution over 600 kPa.

Note that the feature size ratio between the microstructure of the electrode and that of the ionic gel will affect the response-relaxation speed of the sensors. Supplementary Fig. 2 shows the finite element simulations for microstructure contact with feature size ratios of 400%, 200%, and 100% in a loading process. When the feature sizes of the two structures match (feature size ratio ~100%), the two microstructures contact and interlock upon loading. We show that when the feature size ratio approaches to 1, there is substantial interlocking, which is against rapid response-relaxation. When the ratio becomes much larger or smaller than 1, little interlocking is overserved, and response-relaxation time becomes short. Such an effect is evidenced in our experiment (Supplementary Fig. 18). Therefore, the bi-intrafillable structure with a difference in feature size is an ideal selection for rapid, wide-range, and high-sensitivity pressure sensing. The fabrication of the top electrodes and ionic gels with the special microstructures was accomplished through the reverse molding technique (Supplementary Fig. 3). A 45° tilt-view scanning electron microscopy (SEM) image of the microstructured top electrode and the ionic gel film are presented in Fig. 1c, d, respectively, showing that the microstructure of the ionic gel was 2.2 μm, whereas that of the electrode was ~15 μm (Supplementary Fig. 4).

Although both sensors are made of the same materials and similar microstructures, they have different initial states. In an S_n, the ionic gel film is adequately thick to make full contact with the electrode, introducing a large interfacial pressure (P_i), which is critical to its capability to detect a negative pressure (Fig. 1e). An external negative pressure applied to S_n reduces the interfacial contact pressure between the ionic gel and the electrode, leading to a decrease in contact area A and capacitance C. By contrast, S_p uses a thinner ionic gel film so that the electrode is initially not in contact with the ionic gel (Fig. 1f). Such a device can only respond to positive pressures. The assembly process for the two types of sensors (S_n and S_p) are shown in Supplementary Fig. 5.

Preparation and properties of the double network ionic gel

In addition to the design of device structure and microstructures at the interfaces, the performances of the ionic gel are also rationally tailored. Figure 2a shows the preparation of the double network ionic gel with components of (poly(vinylidene-fluoride-co-hexafluoropropylene) (P(VDF-HFP)), polyurethane (PUA)), and an ionic liquid (IL, 1-ethyl-3-methylimida-zolium bis(trifluoromethylsulfonyl)-imid ([EMIM][TFSI])). This double network ionic gel exhibits enhanced crosslinking, enabling the sample to withstand a pressure of 1 MPa without any IL leakage (Fig. 2b).

The double network ionic gel can preserve its resistance over 5000 cycles under a cyclic load of 1 MPa, while that for P(VDF-HFP)-IL has a substantial signal drift (Fig. 2c). This characteristic ensures the

https://doi.org/10.1038/s41467-024-51415-5

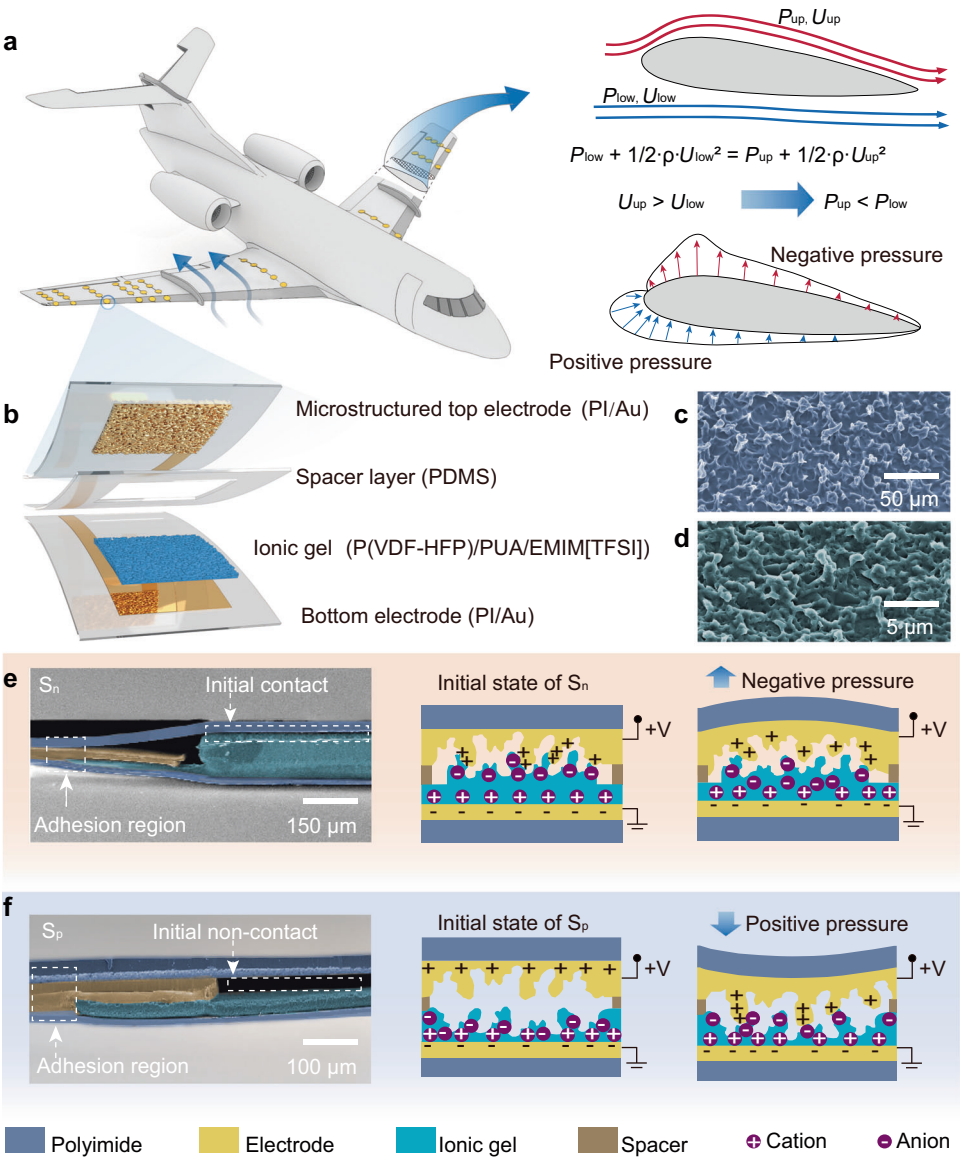

Fig. 1 | Principles of the iontronic sensors for negative and positive pressure measurement. a Schematic diagram of an aircraft equipped with a flexible skin for wind pressure measurement, and the pressure distribution across a wing surface. *P* and *U* represent the wing surface pressure and the wind velocity, respectively, and the Angle symbols 'up' and 'low' represent the upper and lower parts of the wing. **b** Schematic diagram of the structure of the iontronic sensor. **c**, **d** A 45° tilt-view SEM images of (**c**) the top electrode and (**d**) the ionic gel film. **e** SEM images showing the cross-section of S_n, in addition to its sensing mechanism. **f** SEM image showing the cross-section of S_p, and its sensing mechanism.

long-term operational stability of the sensors. Figure 2d shows that the double network ionic gel possesses a maximum fracture energy of 427.1 J·m^{-2}. The uniaxial tensile curves of the double network ionic gel with varied contents of PUA are compared in Fig. 2e, showing that the modulation of Young's modulus in the double network ionic gels can be effectively achieved by increasing the content of PUA (Supplementary Fig. 6). The Young's modulus of the active material is a parameter to balance the sensitivity and working range of sensors. When a maximum compression stress of 1 MPa was applied for 100 cycles, corresponding hysteresis loops almost overlap at the 1st, the 10th, and the 100th cycle, demonstrating high fatigue resistance (Fig. 2f).

Variations in environmental conditions, including relative humidity and temperature, are known to affect material properties. The double network ionic gel exhibits negligible changes in dynamic compression cycles at 12%, 43%, and 98% relative humidity (Fig. 2g). In addition, the double network ionic gel is thermally stable up to 180 °C (Supplementary Fig. 7).

The ionic conductivity and charge density of ionic conductors play a crucial role in the functionality of iontronic sensors. We conduct AC-impedance measurements and measure the Nyquist plot (Fig. 2h) and the Bode phase plot (Supplementary Fig. 8) of the double network ionic gel. By fitting the impedance data to the equivalent circuit model in Fig. 2h and Supplementary Table 1, the capacitance per unit area between the double network ionic gel and the electrode is determined to be 6.32×10^6 pF·cm^{-2}, and the conductivity of the double network ionic gel is 8.07×10^{-2} S·m^{-1}. The conductivity of the double network ionic gel with varying PUA contents is measured using the same method. The experimental results indicate that altering the PUA content in the ionic gel leads to negligible change in its electrical conductivity (Fig. 2i). We select the composition of 10 wt% PUA for a combination of desired mechanical and electrical properties.

https://doi.org/10.1038/s41467-024-51415-5

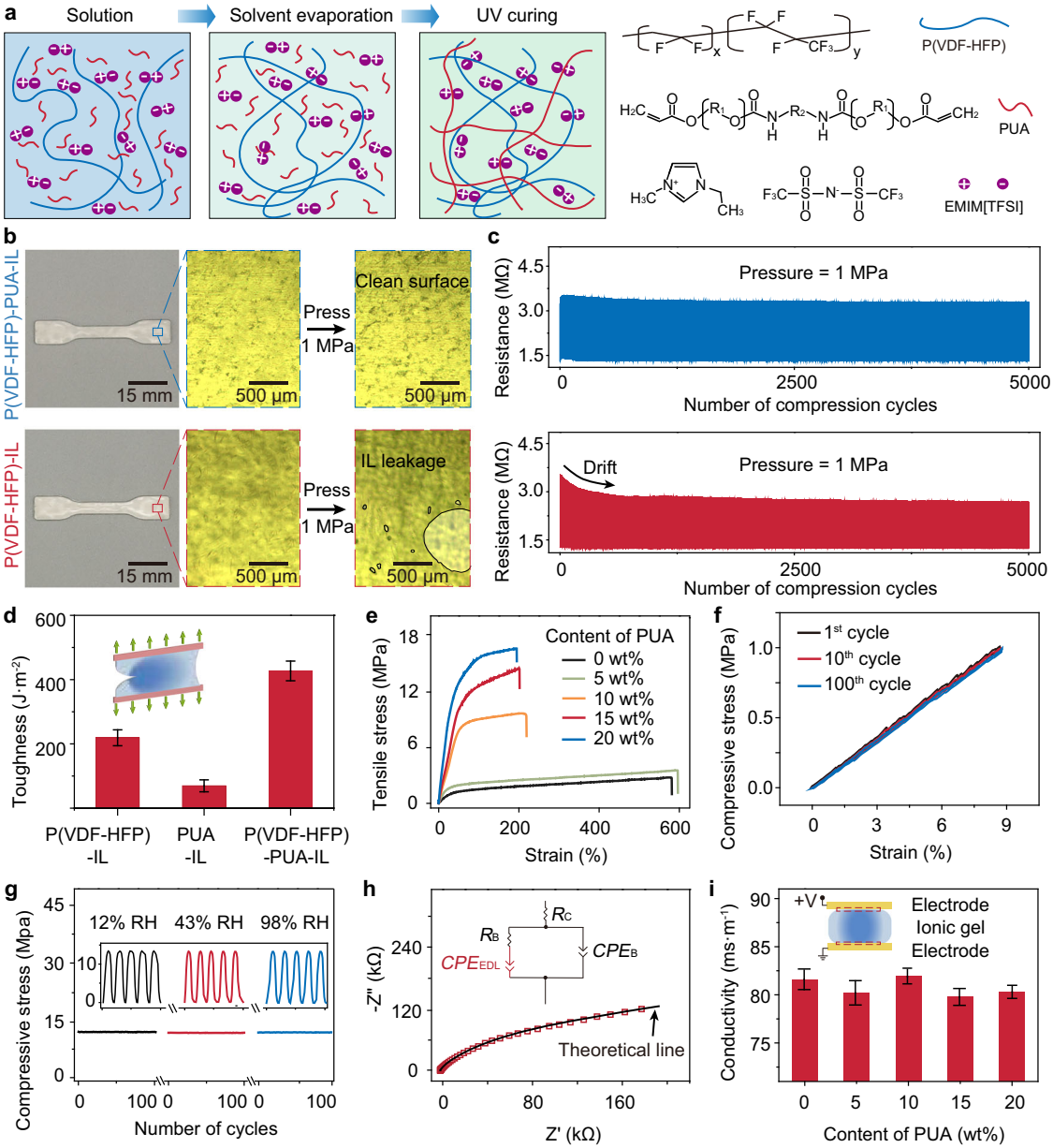

Fig. 2 | Characterization of the double network ionic gel. a Chemical structure of the ionic gel. **b** Photograph of a specimen of the double network ionic gel, along with the optical images of the surface before and after applying a pressure of 1 MPa, showing no ion leakage. P(VDF-HFP)-IL is used as a control sample and ionic leakage occurs upon compression at 1 MPa. **c** Variations of the impedance of the double network ionic gel over 5000 loading-unloading cycles with peak load of 1 MPa. **d** Toughness values of P(VDF-HFP)-IL, PUA-IL, and the double network ionic gel. Error bars represent the standard deviation of three repeated measurements. **e** Uniaxial tensile curves of double network ionic gels with PUA contents of 0 wt%, 5 wt%, 10 wt%, 15 wt%, and 20 wt%. **f** Compressive stress-strain curves of the double network ionic gel of the 1st, 10th, and 100th cycles at a maximum compression stress of 1 MPa, showing negligible fatigue under compression. **g** Variations of the compression stress of the double network ionic gel under relative humidity values of 12%, 43%, and 98%. **h** Nyquist plot of the double network ionic gel. The black line is the theoretical fitting using the equivalent circuit model in the inset. R_C represents the contact resistance, R_B represents the bulk resistance, CPE_B represents the constant phase element of the bulk, and CPE_{EDL} represents the constant phase element of the electric double layer. **i** Conductivity of the double network ionic gels with different PUA contents. Error bars represent the standard deviation of five repeated measurements.

Sensing properties of S_n

The capacitance-to-pressure response of S_n was measured using a specially designed system that consists of a pressure chamber, a pressure gauge, a gas inlet, and an outlet unit equipped with a control valve, as shown in Fig. 3a. The gas inlet equipped with the pressure valve can accurately control the air pressure in the chamber. When the air pressure inside the chamber changes, an LCR meter collects the corresponding capacitance signal and transmits the signal to a PC.

S_n exhibits high sensitivity over a wide pressure range (Fig. 3b). When the negative pressure ranges from 0 to −10 kPa, the sensitivity is 1.60×10^3 pF·kPa^{-1}, and sensitivity increases to 1.69×10^4 pF·kPa^{-1} in the pressure range from −20 to −10 kPa. When the pressure is between −20 and −100 kPa, sensitivity reduces to 1.58×10^3 pF·kPa^{-1}. The lower initial sensitivity is attributed to the partial interlocking of the microstructures, although the difference in the feature sizes of the two structures can relieve the mechanical interlocking. After unlocking, the interfacial contact becomes fully elastic, and thus the sensitivity dramatically increases within −10 and −20 kPa. Sensitivity in the range between −20 and −100 kPa further decreases because of the stiffening of the electrodes. Note that the capacitance-pressure characteristic is

https://doi.org/10.1038/s41467-024-51415-5

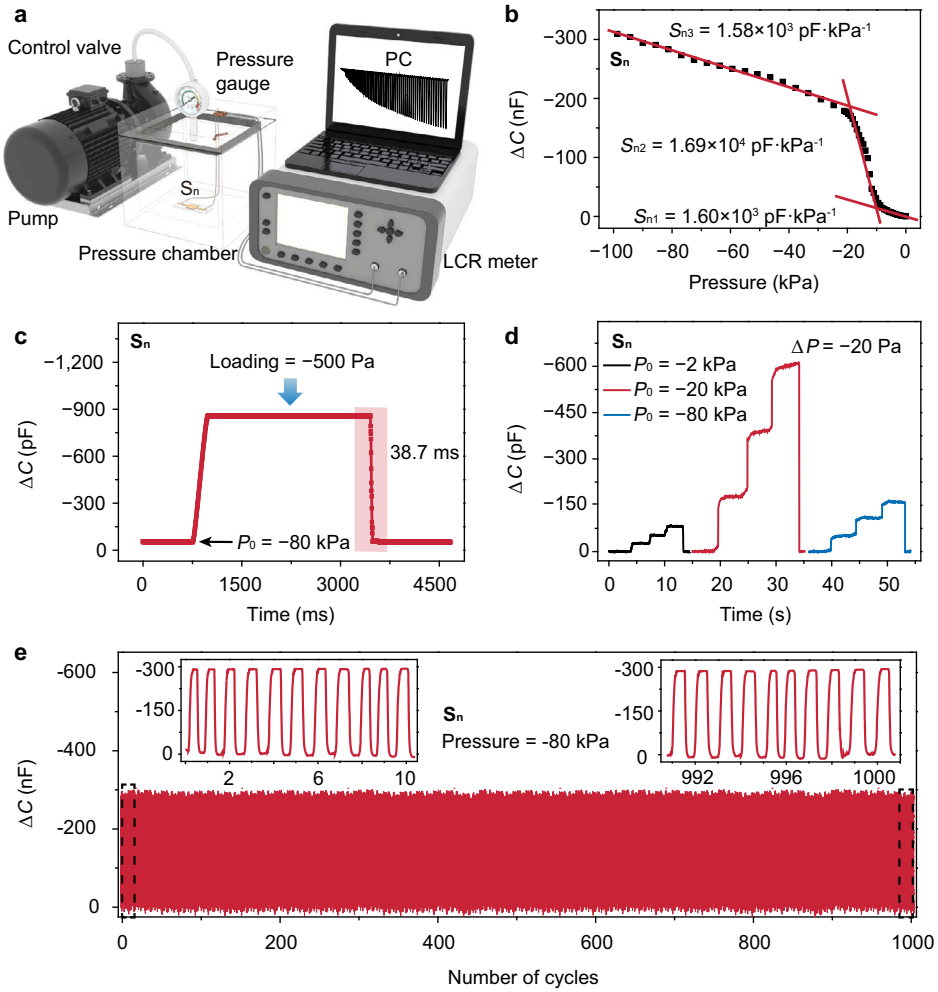

Fig. 3 | Sensing properties of the negative pressure sensor. a Schematic diagram of the measurement setup is used to characterize the sensing properties of S_n. **b** Change in capacitance as a function of pressure. **c** Response of S_n under −80 kPa, showing a relaxation time of 38.7 ms. **d** Response of S_n to a pressure of −20 Pa under different base pressures of −2, −20, and −80 kPa. **e** Repeatability test under cyclic loads from 0 to −80 kPa.

highly repeatable. We measure the curves of ten different samples, showing that the response curves of the three devices are well overlapped (Supplementary Fig. 9). Despite the inherent randomness of the microstructure, an adequate number of microstructures can effectively mitigate performance disparities among different samples.

The relaxation time of the sensor was determined to be 38.7 ms under a pressure (P_0) of −80 kPa (Fig. 3c). It is worth noting that, 38.7 ms includes the operation time of the valve and the running time of the gas in the measuring system. We believe that the true relaxation time of the sensor under high negative pressure is less than 38.7 ms.

In addition, the ultra-sensitive response allows for high pressure-resolution. The smallest pressure-change that the sensor can resolve at a given base pressure is defined as pressure-resolution. We measured the pressure-resolution values at base pressures of −2, −20, and −80 kPa, which belong to the three pressure ranges with different sensitivity values. The measurement was conducted by applying a basic external load on the device, followed by adding a tiny load (by adjusting the inlet flow). Our experiments show that S_n can distinguish −20 Pa in all the three pressure ranges (Fig. 2d), corresponding to 0.025% within the pressure range of −80 kPa. Furthermore, S_n was placed in a closed pipe with a high negative pressure environment and further demonstrated its extraordinary pressure-resolution at high pressures, as shown in Supplementary Fig. 10.

The top and bottom PI substrates were bonded together to achieve a high interfacial strength for high mechanical stability (Supplementary Fig. 11). Such interfacial bonding also helps eliminate signal drift or fluctuation occurred in repeated compression-release cycles at a peak pressure of −80 kPa (Fig. 3e). In a test of 5000 repeated bends at a bending radius of 4.2 mm, S_n exhibits negligible signal drift (Supplementary Fig. 12). Despite initial contact between the electrodes and dielectric layer, the latter can still undergo compression to endure bending deformation in negative pressure sensors. The variation in performance of the S_n on different curvature surfaces are shown in Supplementary Fig. 13. Besides, S_n also shows high stability to the environment with different humidity values (Supplementary Fig. 14a) because of the poor permeability of PI to water and the complete sealing[41,42]. Furthermore, signal magnitude grows as temperature rises due to the enhanced ion mobility at higher temperatures (Supplementary Fig. 14b). The response of S_n to temperatures from 25 °C to 90 °C at 600 kPa, as well as the response as a function of pressure over different temperatures are shown in Supplementary Fig. 14c, d, respectively. Although the sensor exhibits temperature drift, we can use a temperature sensor to calibrate the measured pressure[43]. For room temperature wind tunnel tests, temperature variation is often small and its impact on the signal stability can be ignored.

Sensing properties of S_p

The capacitance-to-pressure curve of S_p is divided into three phases over a pressure range of 600 kPa, which is consistent with our simulation results. Before a pressure is applied, the top electrode is not in

contact with the ionic gel, thus the initial capacitance is only 10 pF due to the air gap in the sensor serving as the dielectric. As pressure increases, contact between the protrusions of the electrode and the ionic gel occurs, resulting in a larger frequency-dependent EDL capacitance. The transition from a low initial air capacitance to iontronic super-capacitance produces an ultrahigh sensitivity in the low-pressure regime, and an average sensitivity of 2.52×10^3 pF·kPa^{-1} is achieved when the pressure is below 50 kPa. The sensitivity decreases to 9.43×10^2 pF·kPa^{-1} in the range of 50–200 kPa, and further to 4.21×10^2 pF·kPa^{-1} as pressure increases to 200–600 kPa. Note that the wide working range can cover the highest air pressure range of commercial aircrafts. The decrease in sensitivity with increasing pressure lies in the stiffening effect of the microstructures. We also observed the high uniformity in sensing properties between different sensors (Supplementary Fig. 15). The responses of S_p to humidity and temperature exhibit a similar trend to that of S_n (Supplementary Fig. 16). The limit of detection (LOD), the pressure-resolution at an unloaded condition, is determined to be 0.05 Pa, which is one of the lowest reported LOD values. The pressure-resolution values of S_p under base pressures of 20, 200, and 400 kPa are presented in Fig. 4c. At the whole range of positive pressure, S_p can effectively identify a pressure increment of 100 Pa, or 0.025%. Further experiments were carried out to demonstrate its capability to resolve a low pressure of 85 Pa at a high pressure of 400 kPa, corresponding to a pressure resolution of 0.02%, as shown in Supplementary Fig. 17. The spikes in the capacitance signal indicate that every small pressure change can be accurately recorded and distinguished.

The rapid response of the sensor to dynamic pressure is desired for aircrafts, because vibrations frequently occur during flight, and we thus measured the response-relaxation speed of the sensor. A short response time of 0.9 ms and a relaxation time of 1.8 ms (Fig. 4d) upon loading (100 kPa) and unloading were determined, which are sufficiently satisfactory to the response speed of aviation pressure devices[26]. The high response-relaxation speed is related to the surface microstructures and the low viscoelasticity of the materials. On one hand, there is a difference in the feature size of the microstructures between the electrode and the ionic gel, which prevents the interlocking of the structures (Supplementary Fig. 2). Therefore, the contacted interface can be quickly separated upon release. Supplementary Fig. 18 show that the sensor with the mismatch of feature size can provide the lower response-relaxation time. On the other hand, the ionic gel exhibits a relatively high Young's modulus of 20 MPa (Supplementary Fig. 6), which indicates a short chain length of the polymer and less energy dissipation caused by the entanglement of the chains.

In addition to the detection of pressure, it is also crucial to detect self-excited buffeting or vibrations, a significant threat to aircraft safety that occur frequently during flight. Traditional methods use two separate sensors for static pressure and vibrations, respectively. Here, our S_p can respond to not only static pressure, but also vibrations up to 400 Hz (Supplementary Fig. 19), which enables the monitoring of many vibrations occurred in aircrafts. In Fig. 4e, we demonstrate that a single sensor can capture superposed signal of a static pressure of 100 kPa and 400 Hz vibrations.

To characterize the high-mechanical durability of the sensor under long-time or cyclic, repeated compression-release test over 10,000 cycles with a peak pressure of 420 kPa was performed, and the sensor exhibits negligible signal drift (Fig. 4f). Furthermore, the stable operation of the sensor on the curved surfaces was also verified, with

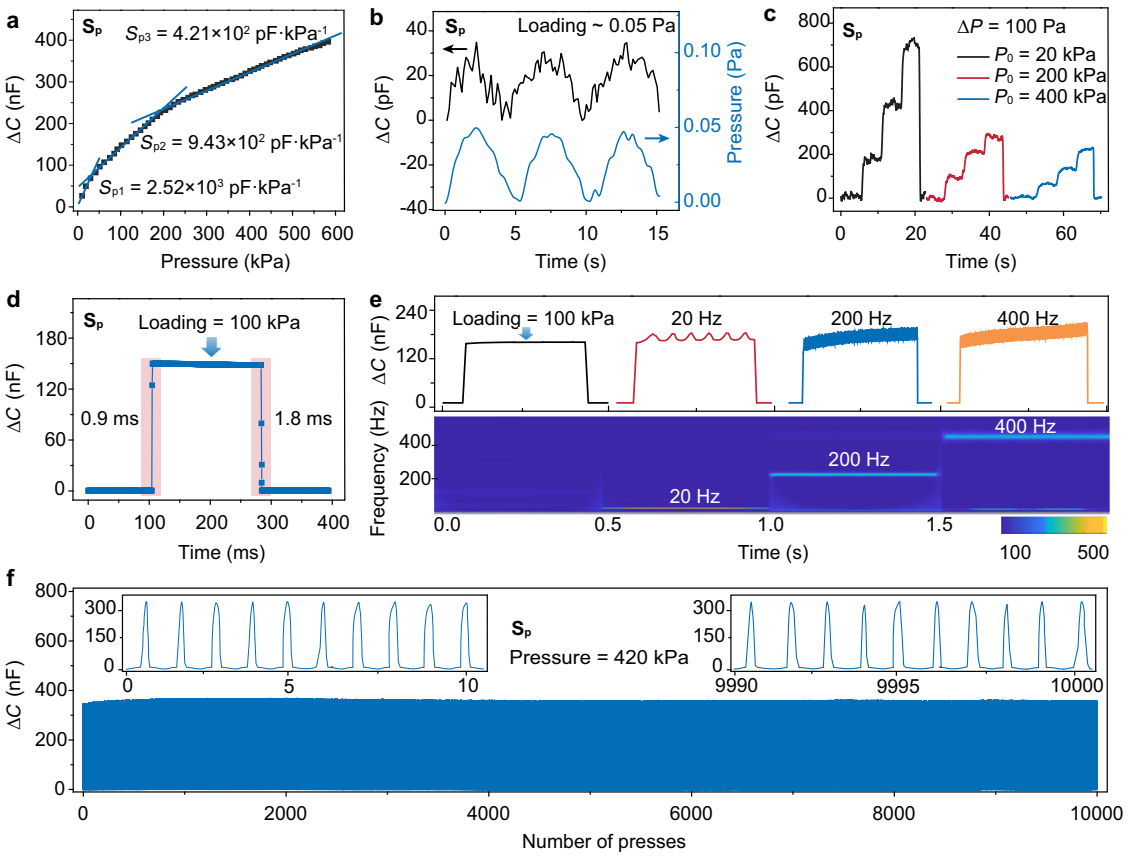

Fig. 4 | Sensing properties of S_p. a Change in capacitance over the pressure range up to 600 kPa. **b** Limit of detection. **c** S_p can resolve a small pressure of 100 Pa under different base pressures of 20, 200, and 400 kPa. **d** Response and relaxation time under a pressure of 100 kPa. **e** Static pressure (100 kPa) detection and vibrations detection with different frequencies of 20, 200, and 400 Hz under a static base pressure of 100 kPa. Corresponding wavelets transform the signals of the vibrations. **f** Working stability tested over 10,000 cycles under a high pressure of 420 kPa.

the sensor maintaining significant mechanical robustness without fatigue after the 5000 bending cycles with a bending radius of 4.4 mm (Supplementary Fig. 20). The high reliability under cyclic bends indicates that the sensor could deform dynamically with the fuselage and wings, and the deformation does not degrade its sensing performance (Supplementary Fig. 21).

Overall, S_n and S_p exhibit high sensitivity and high pressure-resolution over a wide pressure range from −100 kPa to 600 kPa. The high pressure-resolution (−20 Pa for negative pressure sensing and 100 Pa for positive pressure sensing) can satisfy the need of wind tunnel testing (-100 Pa), and the capability to detect high-frequency vibration may enable wing disturbance detection. It signifies that our sensors possess significant potential for applications in different conditions including high-pressure environments, particularly in high-speed trains, aviation, navigation, and related fields. Compared with currently available commercial sensors including MEMS pressure sensors, our sensors are more flexible and thinner, and can be integrated in a thin skin for conformable lamination on curved surfaces.

Wind tunnel experiments for wind pressure measurement

The measurement of air pressure distribution of a wind tunnel model is critical for studying aerodynamic characteristics of an aircraft, such as determining the flow separation points, calculating the aerodynamic loads and lift and drag coefficients, and further optimizing the shape design. The experimental setup of the wind tunnel, which has a length of 245 mm to provide a stable and uniform flow field, is presented in Fig. 5a. A commercial anemobarometer was used to measure the free stream velocities (U_∞) and wind pressure. In particular, the remaining components of the digital conversion area were placed outside the wind tunnel to minimize its impact on airflow. Both negative and positive pressure sensor arrays were laminated along the wing chord direction on the curved surface of a standard airfoil NACA-0012 with a chord length of 150 mm (Fig. 5b), and the sensing units were numbered from N_1 to N_4. It is evident that the sensor arrays can be securely affixed to the wing.

Our iontronic skin can detect AOA or U_∞ values with high reliability. When AOA is fixed at 20° and U_∞ changes from 1.2 $m \cdot s^{-1}$ to 12.5 $m \cdot s^{-1}$, the capacitance change of our sensors and the pressure values measured using a commercial pressure gauge at the leading edge (sensing unit N_2) of the airfoil are shown in Fig. 5c. The sensors are on the leeward side under this AOA and the capacitance values gradually decrease, indicating negative response. The capacitance change (black curve) of our sensors is consistent with that were measured using the commercial pressure gauge (red curve), verifying that our sensor provides reliable measurement.

The sensor can be used for the detection of AOA. Figure 5d shows the real-time capacitance of sensing unit N_2 with AOA changes from 0° to 35° under different U_∞ values. Change in capacitance is observed for each adjustment of AOA with an incremental step of 5°. Specifically,

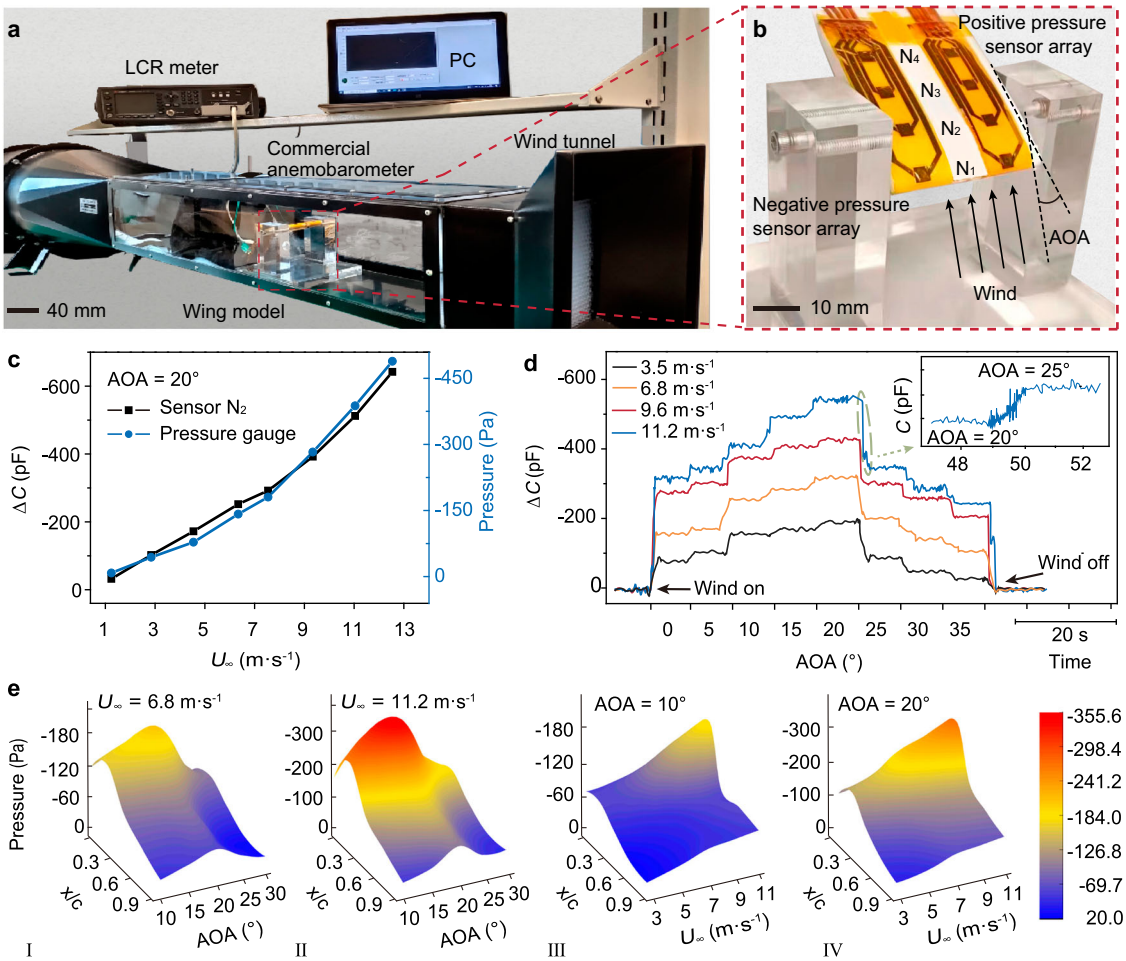

Fig. 5 | Wind tunnel experiments for wind pressure measurement. a Experiment setup and acquisition circuit system. **b** A standard NACA 0012 airfoil mounted with the sensor array. **c** Comparison of measured results between our sensor and commercial pressure gauge with varying U_∞. **d** Real-time capacitance change as a function of AOA of point N_2 under different U_∞ values of 3.5, 6.8, 9.6, and 11.2 $m \cdot s^{-1}$. The inset shows the original data with AOA changing from 20° to 25° when U_∞ is fixed at 11.2 $m \cdot s^{-1}$. **e** Pressure distribution along the normalized wing chord under different AOA and U_∞ values.

the signal can clearly be recognized in the original data with AOA changing from 20° to 25° when U_∞ is fixed at 11.2 m · s^{-1}, corresponding to the capacitance change of only a few picofarads. Under different U_∞ values, the change in capacitance reaches the minimal value when AOA is 20°. As AOA is greater than 20°, the change in capacitance gradually drops because air flow separation forms on the wing surface, reducing the negative pressure at the leading edge. Further experiments were carried out to verify that our sensors can work stably in the wind tunnel model for a long period of time. When AOA is fixed at 20°, the wind tunnel is repeatedly open and closed, resulting in a U_∞ changing from 0 to 11.2 m · s^{-1}, and the capacitance of sensors barely drifts (Supplementary Fig. 22).

The sensor array can also monitor the overall surface pressure distribution along the wing chord by using a multi-channel synchronous acquisition circuit. The circuit consists of a capacitance-digital converter (CDC) chip, a micro-controller board (FPGA), and a wireless transfer module (Supplementary Fig. 23). The capacitance signals collected by the circuit can be converted into pressure through data processing in a PC. Figure 5e presents pressure distribution along the normalized wing chord (x/c) with varying AOA from 10° to 30° at U_∞ values of 6.8 (I) and 11.2 m·s^{-1} (II). The pressure at the front of the wing is higher because of the faster fluid velocities under different U_∞ and AOA values. At $x/c \approx 0.2$ (near sensing unit N_2), the highest pressure appears.

In general, a larger pressure difference of the wing surfaces can provide a higher lift force. The total pressure on the wing surface increases as AOA varies from 10° to 20°. However, after 20°, the total pressure drops with increasing AOA, indicating that severe airflow separation occurs, and the fluid on the wing surface changes from stable and streamlined flow to violent eddy flow. As AOA changes from 10° (Fig. 5e III) to 20° (Fig. 5e IV), the surface pressure distribution varies with the U_∞ in the range from 3 to 11 m·s^{-1}. Under such an AOA and a certain range of U_∞, the pressure values at the position of all sensing units are negative, and thus the total pressure on the wing surface is less than zero. As a result, the fluid exerts an upward lift force on the wing surface. Furthermore, the total pressure on the wing surface increases rapidly with the gradual increase of the U_∞, which indicates that a sufficiently large wind speed is beneficial to improve the lift force for the airplane during the accelerated process. Overall, the coordinated action of U_∞ and AOA, which affect the pressure distribution on the wing surface, can be potentially used to adjust the flight state and stability of the aircraft. Therefore, our flexible sensor array is valuable for the measurement of real-time and spatial distribution of wind pressure on wing surfaces.

Discussion

In summary, we have designed an iontronic skin containing two types of sensors (S_n and S_p) in room temperature wind tunnel tests for the detection of both positive and negative air pressure. The two sensors can work under a wide pressure range covering that used in commercial aircrafts. S_n presents a pressure-resolution of −20 Pa (0.025%) over a broad pressure regime (from −100 kPa to −10 Pa), and S_p exhibits a positive pressure resolution of 100 Pa (0.025%) over an extremely high pressure up to 600 kPa. S_p also has a fast response speed so that it can monitor vibrations with frequencies up to 400 Hz. Furthermore, a flexible sensor arrays incorporating S_n, S_p, and an acquisition circuit were prepared and affixed to the NACA-0012 airfoil, which can in-situ and real-time measure the wing surface pressure and angle of attack in wind tunnel tests. Note that there are a few wind tunnels working at low temperatures down to −50 °C, at which iontronic sensors may not work normally. Fortunately, most wind tunnels operate at room temperature with a nearly constant temperature during the test. Therefore, temperature is not a concern for the pressure measurement with iontronic sensors in such regular wind tunnels. The measurement of aerodynamic parameters using our sensors is expected to be used for the design of aircrafts and other aviation applications.

Methods

Finite element analysis

FEA was performed using the commercial package COMSOL Multiphysics 5.5, which provided the structural mechanics modules with contact deformation and coupled multi-physical fields. The ionic gel with micro-sturctures was modeled as an incompressible neo-Hookean material with Young's modulus (E) ~ 20 MPa according to experimental measurement, was characterized in Supplementary Fig. 6. The PI-Au electrode (E ~ 3 GPa) was simply treated as a rigid plate and compressed downward. All contact interactions were assumed to be friction-less without penetration. In addition, the initial contact area (A_0) of the model in FEA was evaluated at a pressure of 100 Pa.

Preparation of ionic films

A commercial sandpaper (mesh of 10000 #) was used as the template to make microstructures on the surface of ionic gel. Two grams of P(VDF-HFP) (Sigma–Aldrich) was mixed in acetone (Sinopharm Chemical Reagent Co., Ltd), stirring for 2 h at room temperature. After adding 0.2 g of PUA (Shanghai Guangyi Chemical Co., Ltd) and 2 g of [EMIM][TFSI] (Sigma–Aldrich) into the polymer-solvent mixture, the solution was stirred for 30 min to mix completely. The ionic gel film was obtained by dropping the mixed polymer solution onto the sandpaper template and UV light treatment for 1 h. Finally, the as-prepared ionic gel film was peeled off from the sandpaper and cut to desired shapes.

Preparation of the microstructured electrodes

The flexible AU/PI film with microstructures with a thickness of ~40 μm was used as the top electrode, which was obtained by the following steps. Step 1, a prepolymer solution of PDMS was coated on a piece of commercial sandpaper and then cured at 80 °C for 2 h. Step 2, the cured PDMS layer was peeled off from the sandpaper, and used as the template to make microstructured AU/PI electrodes. Step 3, the prepolymer solution of polyimide was casted on the PDMS mold and spun at a speed of 2000 rpm for 30 s using a spin coater (WS-650MZ, MYCRO). Step 4, the precursor solution of the mold was cured at 40 °C for 4 h in an incompletely cured state and then continued to cure completely at 240 °C for 1 h. Step 5, the flexible polyimide (PI) film with microstructures was peeled off, then plasma treated for 30 s and soaked in 2% sodium hydroxide solution for 1 h. Step 6, a layer of gold film (300 nm) was deposited on the prepared PI film at a current of 25 mA for 300 s using an ion sputter (MC1000, Hitachi High-Tech Corporation).

Preparation of the iontronic pressure sensor

The two different types of sensors both consisted of four layers: a bottom electrode layer, a spacer, an ionic gel layer, and a top packaging material with a top electrode.

S_n was assembled in seven steps. Step 1, the flat side of the ionic gel was adhered to the bottom electrode. Step 2, a layer of commercial PDMS (35 μm) was then cut to the square ring with an inner side length of 3 mm and an outer side length of 5 mm serving as the spacer using a laser cutter (WE-6040). Step 3, the encapsulation layer was subjected to plasma treatment for 30 s, to introduce active functional groups onto its surface. Step 4, the spacer was bonded with the bottom layer, with its inner space aligning with the microstructures of the electrode. Step 5, a pre-pressure of 100 kPa was applied to the top electrode area using a machine to establish contact and compression against the ionic gel. Step 6, once the pre-pressure stabilized, the sensor was packaged by applying a pressure (~ 40 kPa) to bond the top layer and the spacer. Step 7, pre-pressure was released. The sensor was ready for use after the seven steps.

S_p was assembled in five steps. Step 1, the flat side of the ionic gel was adhered to the bottom electrode. Step 2, a layer of commercial PDMS (35 μm) was then cut to the square ring with an inner side length of 3 mm and an outer side length of 5 mm serving as the spacer using a laser cutter (WE-6040). Step 3, the encapsulation layer was subjected to plasma treatment for 30 s to introduce active functional groups on its surface. Step 4, the spacer was bonded with the bottom layer, with its inner space aligning with the microstructures of the electrode. Step 5, the sensor was packaged by applying a pressure (~40 kPa) to bond the top layer and the spacer.

Characterization and mechanical measurements

The microstructures of the ionic film were characterized by using field-emission scanning electron microscopy (FE SEM, TESCAN). The AC-impedance spectra were measured using an electrochemical workstation (CHI660E, Shanghai Chenghua Co., LTD) at an amplitude of 500 mV and within the frequency range of 0.1 Hz to 100000 Hz. Thermogravimetric analysis (TGA-DSC1, METTLER TOLEDO) was used for evaluating the thermodegradation of the samples. The capacitance was measured using an LCR meter (E4980AL, KEYSIGHT). The external pressure was applied and measured accurately using a force gauge with a computer-controlled stage (XLD-20E, Jingkong Mechanical Testing Co., Ltd). The bending cycles of the flexible iontronic pressure sensor were evaluated using a smart stretching tester (WS150-100). All other capacitance signals were tested at a frequency of 1 kHz unless otherwise specified, and all sensor size was set to a square with a side length of 5 mm unless otherwise specified.

Reporting summary

Further information on research design is available in the Nature Portfolio Reporting Summary linked to this article.

Data availability

The authors declare that all data supporting the results in this study are present in the paper and the data sources are available at https://doi.org/10.6084/m9.figshare.26393275. All other data supporting the findings of this study are available within the article and its supplementary files. Any additional requests for information can be directed to the corresponding authors.

References

1. Guttag, M., Yan, D. & Reis, P. M. Programmable Aerodynamic Drag on Active Dimpled Cylinders. *Adv. Eng. Mater.* **21**, 1801315 (2019).
2. Terwagne, D., Brojan, M. & Reis, P. M. Smart morphable surfaces for aerodynamic drag control. *Adv. Mater.* **26**, 6608–6611 (2014).
3. Ding, F. & Kareem, A. Tall Buildings with Dynamic Facade Under Winds. *Engineering* **6**, 1443–1453 (2020).
4. Turjo, I. & Lipsett, M. G. Retrofitting Health and Usage Monitoring Systems (HUMS) for Unmanned Aerial Vehicles. *IEEE Aerosp. Electron. Syst. Mag.* **18**, 2506–2510 (2023).
5. Ajanic, E., Feroskhan, M., Mintchev, S., Noca, F. & Floreano, D. Bioinspired wing and tail morphing extends drone flight capabilities. *Sci. Robot.* **5**, eabc2897 (2020).
6. Yuan, S., Wang, H. & Chen, J. A PZT Based On-Line Updated Guided Wave - Gaussian Process Method for Crack Evaluation. *IEEE Sens. J.* **20**, 8204–8212 (2020).
7. He, J., Huo, H., Guan, X. & Yang, J. A Lamb wave quantification model for inclined cracks with experimental validation. *Chin. J. Aeronaut.* **34**, 601–611 (2021).
8. Yin, F., Ye, D., Zhu, C., Qiu, L. & Huang, Y. A. Stretchable, Highly Durable Ternary Nanocomposite Strain Sensor for Structural Health Monitoring of Flexible Aircraft. *Sensors* **17**, 327–332 (2017).
9. Liu, W. et al. An Intelligent Robotic System Capable of Sensing and Describing Objects Based on Bimodal, Self-Powered Flexible Sensors. *Adv. Funct. Mater.* **38**, 2309109 (2023).
10. Xu, C. et al. Flexible Pressure Sensors in Human-Machine Interface Applications. *Small* **15**, e2306655 (2023).
11. Ma, X. et al. Highly sensitive, ultra-reliable flexible piezoelectret sensor for non-contact sitting motion tracking and physiological signal monitoring. *Nano Energy* **111**, 108157 (2023).
12. Long, Y. et al. Super-Stretchable, Anti-Freezing, Anti-Drying Organogel Ionic Conductor for Multi-Mode Flexible Electronics. *Adv. Funct. Mater.* **33**, 2304205 (2023).
13. Hammock, M. L., Chortos, A., Tee, B. C. K., Tok, J. B. H. & Bao, Z. The Evolution of Electronic Skin (E-Skin): A Brief History, Design Considerations, and Recent Progress. *Adv. Mater.* **25**, 5997–6037 (2013).
14. Wang, Y., Qiu, L., Luo, Y. J. & Ding, R. A stretchable and large-scale guided wave sensor network for aircraft smart skin of structural health monitoring. *Struct. Health Monit.* **20**, 861–876 (2021).
15. An, L. et al. Soft sensor for measuring wind pressure. *Int. J. Mech. Sci.* **141**, 386–392 (2018).
16. Downey, A., Laflamme, S. & Ubertini, F. Experimental wind tunnel study of a smart sensing skin for condition evaluation of a wind turbine blade. *Smart Mater. Struct.* **26**, 357–362 (2017).
17. Chin, Y. W. et al. Efficient flapping wing drone arrests high-speed flight using post-stall soaring. *Sci. Robot.* **5**, eabc8801 (2020).
18. Ragni, D., van Oudheusden, B. W. & Scarano, F. Non-intrusive aerodynamic loads analysis of an aircraft propeller blade. *Exp. Fluids* **51**, 361–371 (2011).
19. Kuester, M. S., Borgoltz, A. & Devenport, W. J. Pressure tap effects on the lift measurement of an airfoil section. *Aerodyn. Meas. Technol. Ground Test. Conf.* **6**, 3654 (2016).
20. Kopsaftopoulos, F., Nardari, R., Li, Y. H., Wang, P. C. & Chang, F. K. Stochastic global identification of a bio-inspired self-sensing composite UAV wing via wind tunnel experiments. *Proc. SPIE Int. Soc. Opt. Eng.* **8**, 5564 (2016).
21. Gregory, J. W., Sakaue, H., Liu, T. S. & Sullivan, J. P. Fast Pressure-Sensitive Paint for Flow and Acoustic Diagnostics. *Annu. Rev. Fluid Mech.* **46**, 2287 (2014).
22. Li, H. C. et al. Wearable skin-like optoelectronic systems with suppression of motion artifacts for cuff-less continuous blood pressure monitor. *Natl Sci. Rev.* **7**, 849–862 (2020).
23. Wada, D. et al. Flight demonstration of aircraft wing monitoring using optical fiber distributed sensing system. *Smart Mater. Struct.* **28**, 749–755 (2019).
24. Buder, U. et al. Family of micromachined wall hot-wire sensors on polyimide foil. *Aiaa. J.* **45**, 1798–1809 (2007).
25. Ngo, L., Kupke, W. & Seidel, H. Simulation and experimental results of a hot-film anemometer array on a flexible substrate. *Proc. CANEUS Conf. Micro Nano Tech.* **10**, 6726 (2006).
26. Huang, Y. et al. Flexible smart sensing skin for "Fly-by-Feel" morphing aircraft. *Sci. China Technol. Sci.* **65**, 1–29 (2022).
27. Shin, H. S. et al. Bio-Inspired Large-Area Soft Sensing Skins to Measure UAV Wing Deformation in Flight. *Adv. Funct. Mater.* **31**, 2105268 (2021).
28. Sun, J., Guan, Q., Liu, Y. & Leng, J. Morphing aircraft based on smart materials and structures: A state-of-the-art review. *J. Intel. Mat. Syst. Str.* **27**, 2289–2312 (2016).
29. Nie, B., Xing, S., Brant, J. D. & Pan, T. Droplet-based interfacial capacitive sensing. *Lab Chip* **12**, 1110–1118 (2012).
30. Zhu, Z., Li, R. & Pan, T. Imperceptible Epidermal-Iontronic Interface for Wearable Sensing. *Adv. Mater.* **30**, 2071652 (2018).
31. Cho, S. et al. Micropatterned Pyramidal Ionic Gels for Sensing Broad-Range Pressures with High Sensitivity. *ACS Appl. Mater. Interfaces* **9**, 10128–10135 (2017).
32. Nie, B., Li, R., Cao, J., Brandt, J. D. & Pan, T. Flexible Transparent Iontronic Film for Interfacial Capacitive Pressure Sensing. *Adv. Mater.* **27**, 6055–6062 (2015).

33. Nie, B., Li, R., Brandt, J. D. & Pan, T. Iontronic microdroplet array for flexible ultrasensitive tactile sensing. *Lab Chip* **14**, 1107–1116 (2014).
34. Chang, Y. et al. First Decade of Interfacial Iontronic Sensing: From Droplet Sensors to Artificial Skins. *Adv. Mater.* **33**, e2003464 (2021).
35. Sun, J.-Y., Keplinger, C., Whitesides, G. M. & Suo, Z. Ionic Skin. *Adv. Mater.* **26**, 7608–7614 (2014).
36. Keplinger, C. et al. Stretchable, Transparent, Ionic Conductors. *Science* **341**, 984–987 (2013).
37. Bai, N. et al. Graded intrafillable architecture-based iontronic pressure sensor with ultra-broad-range high sensitivity. *Nat. Commun.* **11**, 209 (2020).
38. Su, Q. et al. Highly sensitive ionic pressure sensor based on concave meniscus for electronic skin. *J. Micromech. Microeng.* **30**, 307–311 (2020).
39. Chen, R. et al. Nonlinearity synergy: An elegant strategy for realizing high-sensitivity and wide-linear-range pressure sensing. *Nat. Commun.* **14**, 6641 (2023).
40. Zhao, J. et al. Carbon Nanotube Network Topology-Enhanced Iontronic Capacitive Pressure Sensor with High Linearity and Ultrahigh Sensitivity. *ACS Appl. Mater. Interfaces* **15**, 47327–47337 (2023).
41. Chen, G. Q., Scholes, C. A., Qiao, G. G. & Kentish, S. E. Water vapor permeation in polyimide membranes. *J. Memb. Sci.* **379**, 479–487 (2011).
42. Huang, J., Cranford, R. J., Matsuura, T. & Roy, C. Water vapor sorption and transport in dense polyimide membranes. *J. Appl. Poly. Sci.* **87**, 2306–2317 (2003).
43. Ramanathan, A. & Headings, L. Differential pressure sensor using flexible piezoelectrics with pyroelectric compensation. *Smart. Mater. Struct.* **30**, 035020 (2021).

Acknowledgements

This work is supported by the National Key Research and Development Program of China (No. 2022YFB3203600), National Natural Science Foundation of China (no. T2225017, 52075432, and 52073138), and Science Technology and Innovation Committee of Shenzhen Municipality No. JCYJ20210324120202007.

Author contributions

C.F.G., X.W. and J.W. conceived the idea and designed the research. C.F.G. and J.W. performed most of the experiments. Y.C. and J.W. conducted the simulation. J.W, J.S. and N.B. analyzed the sensing properties. B.L. designed the signal acquisition system and X.W. prepared the circuit. C.F.G., X.F.W. Y.C. and Z.J. drafted the manuscript, and all authors contributed to the writing of the manuscript.

Competing interests

The authors declare no competing interests.

Additional information

Supplementary information The online version contains supplementary material available at https://doi.org/10.1038/s41467-024-51415-5.

Correspondence and requests for materials should be addressed to Xueyong Wei, Yingchun Chen or Chuan Fei Guo.

Peer review information *Nature Communications* thanks Dezhi Wu, and the other, anonymous, reviewer(s) for their contribution to the peer review of this work. A peer review file is available.

Reprints and permissions information is available at http://www.nature.com/reprints

Publisher's note Springer Nature remains neutral with regard to jurisdictional claims in published maps and institutional affiliations.

Open Access This article is licensed under a Creative Commons Attribution-NonCommercial-NoDerivatives 4.0 International License, which permits any non-commercial use, sharing, distribution and reproduction in any medium or format, as long as you give appropriate credit to the original author(s) and the source, provide a link to the Creative Commons licence, and indicate if you modified the licensed material. You do not have permission under this licence to share adapted material derived from this article or parts of it. The images or other third party material in this article are included in the article's Creative Commons licence, unless indicated otherwise in a credit line to the material. If material is not included in the article's Creative Commons licence and your intended use is not permitted by statutory regulation or exceeds the permitted use, you will need to obtain permission directly from the copyright holder. To view a copy of this licence, visit http://creativecommons.org/licenses/by-nc-nd/4.0/.

© The Author(s) 2024